Bioimpedance single cell sensing of low and high density sickle erythrocytes using microfluidics

Tieying Xu, Maria Lizarralde-Iragorri, Benoit Charlot, Jean Roman, Olivier Français, Wassim El Nemer, Bruno Le Pioufle

10 (2022) 100140

Contents lists available at ScienceDirect

Biosensors and Bioelectronics: X

journal homepage: www.journals.elsevier.com/biosensors-and-bioelectronics-x

Bioimpedance single cell sensing of low and high density sickle erythrocytes using microfluidics

Tieying Xu [a,b], Maria A. Lizarralde-Iragorri [c,d,e], Benoit Charlot [b], Jean Roman [a], Olivier Français [a,f,1], Wassim El Nemer [c,d,e,g,h,1], Bruno Le Pioufle [a,i,*,1]

[a] Université Paris-Saclay, ENS Paris-Saclay, CNRS, Institut d'Alembert, F-91190, Gif sur Yvette, France
[b] IES, Université de Montpellier, CNRS, F-34090, Montpellier, France
[c] Université de Paris, UMR_S1134, BIGR, Inserm, F-75015, Paris, France
[d] Institut National de Transfusion Sanguine, F-75015, Paris, France
[e] Laboratoire d'Excellence GR-Ex, F-75013, Paris, France
[f] ESYCOM, Univ Gustave Eiffel, CNRS UMR 9007, F-77454, Marne-la-Vallee, France
[g] Etablissement Français du Sang PACA-Corse, F-13005, Marseille, France
[h] Aix Marseille Univ, EFS, CNRS, ADES, "Biologie des Groupes Sanguins", F-13005, Marseille, France
[i] Université Paris-Saclay, ENS Paris-Saclay, CNRS, Institut d'Alembert, LUMIN, F-91190, Gif sur Yvette, France

ARTICLE INFO

Keywords:
Sickle cell disease
Red blood cells
Bioimpedance
Microfluidics
Single cell analysis

ABSTRACT

In this paper, sickled red blood cells of different densities from distinct Sickle Cell Disease (SCD) patients were analyzed, using a microfluidic device based on bioimpedance sensing. Complementary to our previous work (Xu et al., 2020) demonstrating the capacity of our microfluidic device to discriminate between normal and pathological red blood cells, we investigated the microcirculatory properties of red blood cells (RBCs) in sickle cell disease based on their density. RBCs were separated using a triple density Percoll fractionation in low density (LD), dense (D) and high density (HD) RBCs. Single cell transiting through microfluidic constrictions was electrically recorded. Gaussian distributions, adjusted to the histograms of transit time (TT), as well as in phase blockade amplitude (IP BA) and phase shift (PS) of the electrical signal, were analyzed for the three RBC subpopulations. A specific electrical signature was achieved for each RBC subpopulation, with decreased TT, BA and PS for increasing densities. This approach provides a promising tool to monitor the effect of therapeutical strategies in sickle cell disease and other red cell disorders.

1. Introduction

Sickle cell disease (SCD) is a hemolytic anemia characterized by painful vaso-occlusive crises (VOCs) due to the obstruction of small blood capillaries (Pauling et al., 1949) (Ballas et al., 2012). The mutation in the gene encoding β globin chain leads to the production of abnormal hemoglobin (HbS), which polymerizes under hypoxic conditions causing the sickling of red blood cells (RBCs) (Steinberg, 2008) (Stuart and Nagel, 2004). In SCD, RBC properties are irreversibly altered, with increased cellular dehydration, rigidity and fragility (Piel et al., 2017) (Ware et al., 2017). Based on *in vivo* studies using SCD mouse models, VOCs would be initiated by abnormal adhesion of neutrophils or of young RBCs, called reticulocytes (Bookchin et al., 1991) (Swerlick et al., 1993) (Gee and Platt, 1995), to the capillary wall reducing its luminal diameter, followed by obstruction with rigid dense RBCs. Studies with human RBCs are more difficult to achieve *in vivo*, but several *in vitro* studies show marked differences among the heterogeneous RBC population in SCD. To access SCD RBC microcirculatory properties at a single cell level, we have recently developed a miniaturized bioimpedance-microfluidic device that mimics the dimensions of human capillaries (Toepfner et al., 2018) (Varlet-Marie et al., 2010) (Liu et al., 2019) and induces successive mechanical constraints on flowing RBCs. Physical parameters related to RBC microfluidic transiting within a 30 μm long section of 5 μm × 2 μm, in which RBCs are squeezed, were measured (Fig. 1A., B., C. and D.) (Hoffman and Britt, 1979) (Gawad et al., 2001) (Zhou et al., 2018). We demonstrated that this device was able to discriminate between normal and pathological RBCs based on their rigidity and capacity to deform (Xu et al., 2020). Conventional

* Corresponding author. 4 Avenue des Sciences, 91190, Gif-sur-Yvette, France.
E-mail address: bruno.le-pioufle@ens-paris-saclay.fr (B. Le Pioufle).
[1] These authors contributed equally.

https://doi.org/10.1016/j.biosx.2022.100140
Received 19 January 2022; Received in revised form 16 March 2022; Accepted 3 April 2022
Available online 13 April 2022

methods to analyze RBC populations, as Cytometry do not offer the capabilities to analyze single cell in physiological conditions (constrained with a biomimicking capillary) (Piagnerelli et al., 2006). Optical tweezers is a good alternative to analyze the single cell bio-rheological properties (Zhu et al., 2020), nevertheless with low throughput. The microfluidic approach gives a good compromise (Amirouche et al., 2020) (Man et al., 2021) (Zheng et al., 2013) as it allows to achieve the single cell sensing in physiological conditions, with possible high throughput when electrical sensing is integrated, as in our case (Supplementary Table 1.).

In this paper, RBCs from SCD patients were separated into 3 subpopulations using a triple density gradient, low density (LD), dense (D) and high density (HD) RBCs (Kaul et al., 1983), and were electrically monitored while flowing in the microfluidic device. Our study shows for the first time that transit time, IP blockade amplitude, and phase shift induced by single RBC transiting can provide an electrical signature of SCD RBCs densities.

2. Material and methods

The miniaturized system proposed for experiments was made by the assembly of two subsystems: a fluidic subsystem involving a successive microfluidic open-channels network, manufactured with polydimethylsiloxane (PDMS) polymer (Lizarralde Iragorri et al., 2018), and an electrical monitoring subsystem involving gold microelectrodes (Cr 20 nm/Au 200 nm) patterned on a quartz substrate (Xu et al., 2020). Both subsystems were reversibly assembled by depressurization in the channel, that also served to introduce the blood in the microfluidic device. The PDMS part was coated by a parylene C layer (3.5 μm) that prevents any gaz penetration to the channel that would otherwise be caused by the porosity of PDMS. The microfluidic network containing 8 sets of 24 parallel microfluidic channels array (each of those containing 10 successive restrictions) was replicated by soft lithography (Whitesides, 2006) using a three-layers SU-8 resist mold. The total hydraulic resistance of the system was $R_{h\_total} = 1.3 \times 10^{-3}$ Pa·s·μm^{-3} (Oh et al., 2012) (See Fig. 1B.). The subsystem with microelectrodes was manually aligned with the microfluidic network, and reversibly assembled using depressurization. For our experiment a pair of electrodes was aligned with a restriction of the external branch (See Fig. 1C. and D.) (Roman et al., 2018) (Raillon et al., 2013) (Reichel et al., 2019). Excitation voltages $V_{ex}(t) = \hat{V}_{ex} \sin(2\pi f_{ex} t)$ were applied to those electrodes (2 V, 10 kHz) using the transimpedance amplifier AD847J (Analog Discovery), that also sampled the current flowing in the restriction: $I(t) = \hat{I} \sin(2\pi f_{ex} t + \varphi)$, dependent on the cell position within the channel (See Supplementary Figure 1A.). φ is the phase shift introduced by the presence of the cell ($\varphi = 0$ when there is no cell within the restriction). Thanks to synchronous detection system, followed by threshold detection with IGOR Pro software, the IP blockade amplitude $I_{nc} - I_c \cos(\varphi)$ was determined. I_{nc} and I_c correspond respectively to $\hat{I}$ with or without the cell in the restriction. AxioObserver Z1 microscope (Zeiss) was used with a Phantom Miro M 320 S high-speed camera for imaging the cell transit simultaneously to the electrical acquisition (See Supplementary Figure 1B.). Three different blood samples form sickle cell patients non-treated with hydroxyurea (HU) and non-transfused in the previous three months were collected at the hospital "Hôpital Necker-Enfants Malades". RBCs were washed 3 times with ID-CellStab (Biorad), centrifuged at 1500 rpm for 5 min at room temperature, and diluted to 2% hematocrit in conductive buffer (HBSS-BSA 0.4%, 1 mM $CaCl_2$, 1 mM $MgCl_2$, 1.26 Sm^{-1}, 1% F.S. to 1.99 Sm^{-1}).

Sickle cell Percoll fractionation: The RBC suspension was layered at the top of the Percoll gradient layers with densities of 1.076, 1.096, 1.11 g/ml (Specific volumes of two stock solutions allow these densities to be prepared. *Solution 1*: 9.5 ml 0.5 M BSA/H_2O + 0.5 ml Hepes pH 8; *Solution 2*: 9.5 ml 0.5 M BSA/Percoll +0.4 ml Hepes pH 7.3 + 0.1 ml H_2O [Percoll SIGMA-ALDRICH/BSA Euromedex]) (See Supplementary Fig. 2.). Cell fractionation was achieved by a 30 min centrifugation at 1000*g* at room temperature in a swinging-bucket centrifuge (Eppendorf 5804 R). The top layer consisting of the remaining white blood cells was removed and the successive layers, named as LD (low density, rich in reticulocytes), D (dense) and HD (high density, rich in irreversibly sickled cells), were collected, washed 3 times with ID-CellStab to remove Percoll residues, and used for subsequent experiments. The RBCs were obtained from a blood sample collected in a EDTA vacutainer tube.

3. Results and discussion

Sicke RBCs samples obtained from three patients were analyzed in our microfluidic device. Each of those RBCs were fractionated on a triple-density gradient to obtain three populations: low density (LD), dense (D) and high density (HD) RBCs. The nine samples were processed

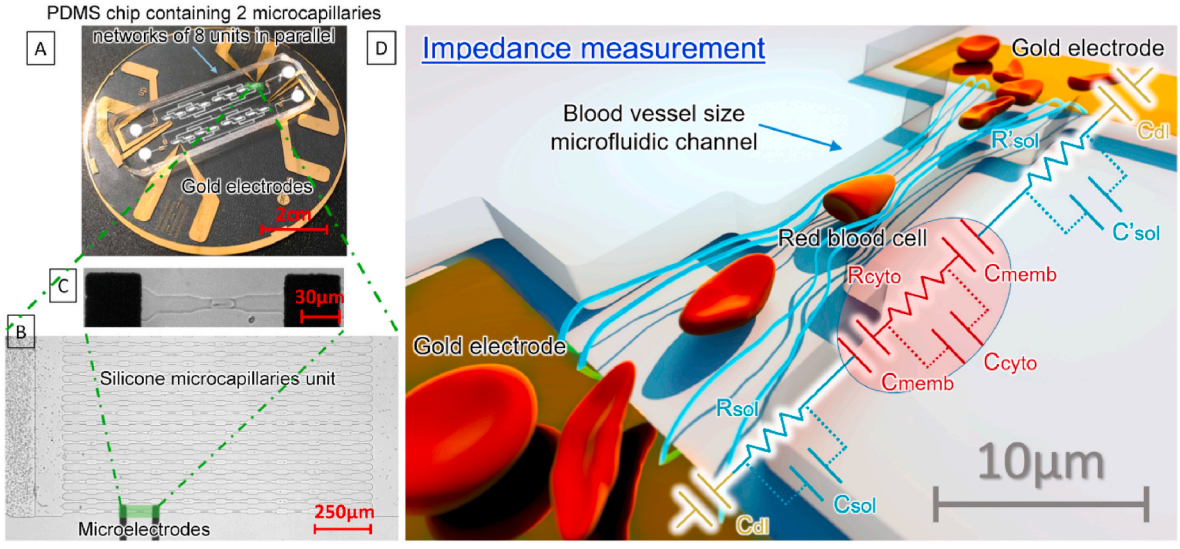

Fig. 1. A. Reversible assembly of the microfluidic channels network and the subunit containing gold electrodes for the sensing of single red blood cell transit; B. Cells transiting within the zone of the 24 channels × 10 restrictions array; C. Single red blood cell transiting within the restriction; D. 3D representation, of the sickled red blood cell transiting between excitation electrodes. (For interpretation of the references to color in this figure legend, the reader is referred to the Web version of this article.)

in the device (40 min flowing duration). A total of 1937 LD (943 from first, 717 from second and 277 from third patient), 2631 D (1063 from first, 1104 from second and 464 from third patient) and 3854 HD RBCs (1682 from first, 1384 from second and 788 from third patient) were analyzed.

Physical parameters associated with the cell microcirculatory properties, which are transit time, IP blockade amplitude and phase shift, were recorded at a single cell level. The Gaussian distribution of these parameters was fitted with a multipeak Gaussian model in order to estimate the mean values (μ_1, μ_2 …) and the dispersions (σ_1^2, σ_2^2 …) for each subpopulation (Roman et al., 2018) (Raillon et al., 2013):

$$y(x) = A1 \cdot e^{-\left(\frac{x-\mu_1}{2\sigma_1^2}\right)^2} + A2 \cdot e^{-\left(\frac{x-\mu_2}{2\sigma_2^2}\right)^2} + \ldots$$

where Ai correspond to the maximum amplitude for each peak in the distribution. Scatter plots were realized to discriminate SCD subpopulations and analyze the interdependency between two of these three parameters.

3.1. Case of transit time

The highest mean transit time was observed for LD RBCs, and decreased inversely to the cell density (μ_{LD_t1} = 11.5 ms, μ_{D_t1} = 9 ms, μ_{HD_t} = 7.4 ms, see Fig. 2A., Supplementary Figure 3A., B., C., Supplementary Table 2.). In addition, the main peak of the LD RBCs showed higher dispersion than the peaks of the D and HD RBCs ($\sigma^2_{LD\_t1}$ = 12.6 ms^2, $\sigma^2_{D\_t1}$ = 4.43 ms^2, $\sigma^2_{HD\_t}$ = 4.47 ms^2, Supplementary Table 2.), indicating a higher variability in this population.

Transit time is dependent on the contact surface between the flowing RBC and the microchannel wall. As HD RBCs are dehydrated and/or sickled cells, they are more elongated than LD and D RBCs (Fig. 2.), with a trend to align with the flow direction. This leads to a smaller contact surface, and thus a shorter transit time (Reichel et al., 2019). At the opposite, LD RBC subpopulation is composed of a majority of reticulocytes (young immature RBCs), which are larger than mature RBCs. LD RBCs present a larger contact surface with the microchannel wall leading to a longer transit time. Therefore, despite the decreased RBC deformability with increasing density, the smaller transit time of HD RBCs appears to be poorly dependent on the cell deformability and mostly governed by the dominant effect of decreased contact surface at this particular microchannel size.

The multipeak behavior in Fig. 2. is related to the heterogeneity (size, shape) in the same subpopulation. Indeed, LD RBC subpopulation is composed of a majority of reticulocytes (young immature RBCs), which are larger than mature RBCs, leading to a longer mean transit

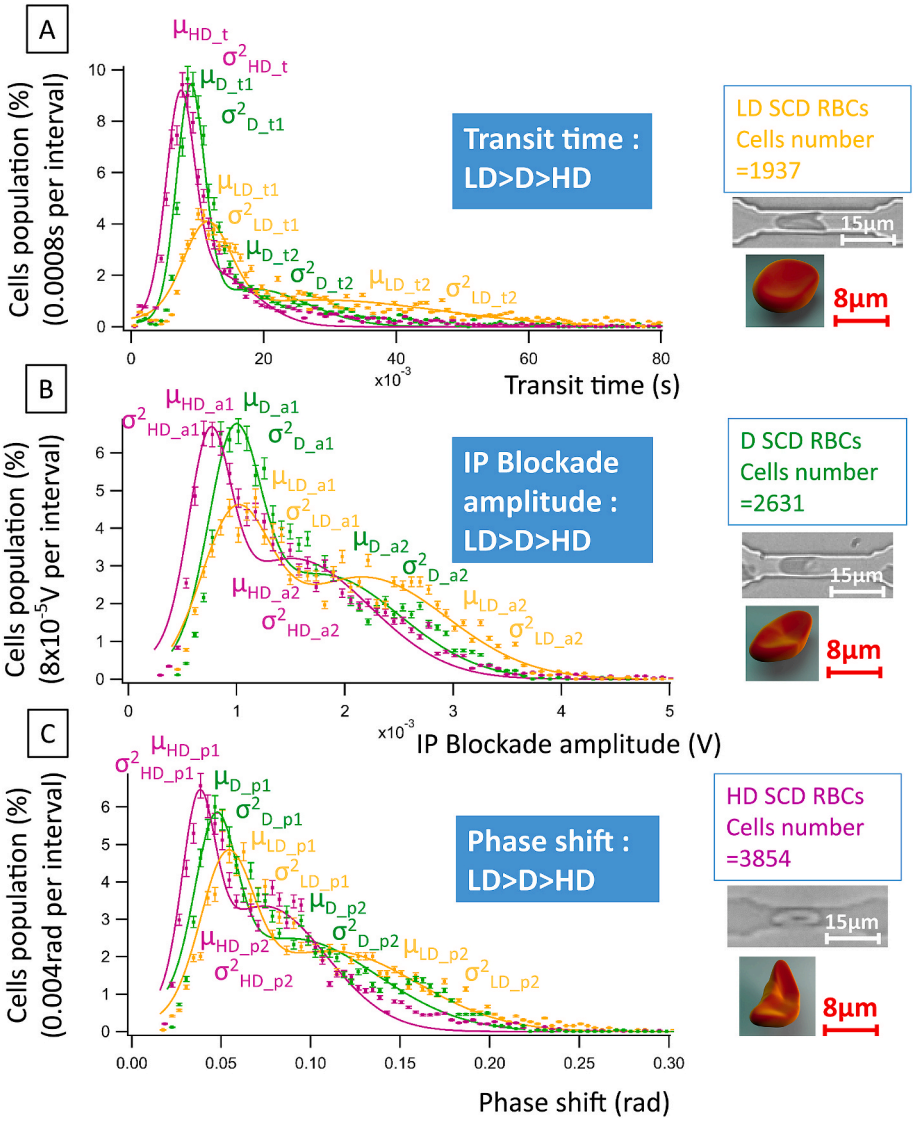

Fig. 2. Gaussian distributions, adjusted to histogram (See Supplementary Fig. 3, 4 and 5.), of transit time, of IP blockade amplitude and of phase shift measured for each subpopulation of three non-treated SCD patients. Microscopy imaging of the cell transit performed simultaneously to the electrical recording. The error bar represents 5% of the value. 3D reconstitution, according to measurement data (See Supplementary Table 5.), representing separately their sickle shape of different levels (Lizarralde Iragorri et al., 2018). A. Comparison of the Gaussian distribution of transit time, adjusted to histogram, for 1937 sickled red blood cells of low density (orange curve for LD SCD RBCs), for 2631 sickled dense red blood cells (green curve for D SCD RBCs) and for 3854 sickled red blood cells of high density (violet curve for HD SCD RBCs); B. Comparison of the Gaussian distribution of IP blockade amplitude, adjusted to histogram, for LD, D and HD SCD RBCs subpopulations; C. Comparison of the Gaussian distribution of phase shift, adjusted to histogram, for LD, D and HD SCD RBCs subpopulations. (For interpretation of the references to color in this figure legend, the reader is referred to the Web version of this article.)

time and a higher IP blockade amplitude.

3.2. Case of IP blockade amplitude

The in phase amplitude of the electrical current blockade also decreased with increasing RBC density (μ_{LD_a1} = 0.979 mV, μ_{D_a1} = 0.976 mV, μ_{HD_a1} = 0.8 mV, see Fig. 2B., Supplementary Figure 4A., B., C., Supplementary Table 3.), confirming our interpretation regarding the major influence of the decreasing contact surface of RBC with the microchannel walls, with increasing densities. The IP blockade amplitude distribution appears to be dispersed, which can be attributed to variability of RBC morphology for each subpopulation as well as various possible positions of the cell during its transit through the restricted fluidic channel.

3.3. Case of phase shift

As the presence of the cell interfers with the electrical field topology between the sensing electrodes, a phase shift between the applied voltage and induced current produced by the microelectrodes can also be measured. This phase shift reflects the presence of RBC squeezed within the smallest section of the microchannel. The mean value of phase shift decreased with increasing density (μ_{LD_p1} = 0.053 rad, μ_{D_p1} = 0.047 rad, and μ_{HD_p1} = 0.037 rad, see Fig. 2C., Supplementary Figure 5A., B., C., Supplementary Table 4.).

Analytical prediction of phase shift, varying with RBC density (reflected by different membrane permeabilities, contact surfaces and membrane thickness), was also achieved (Supplementary Fig. 6.). With the consideration of RBC membrane thickness (e_{memb} = 8 nm) (Singer and Nicolson, 1972) (Hochmuth et al., 1983) (Heinrich et al., 2001),

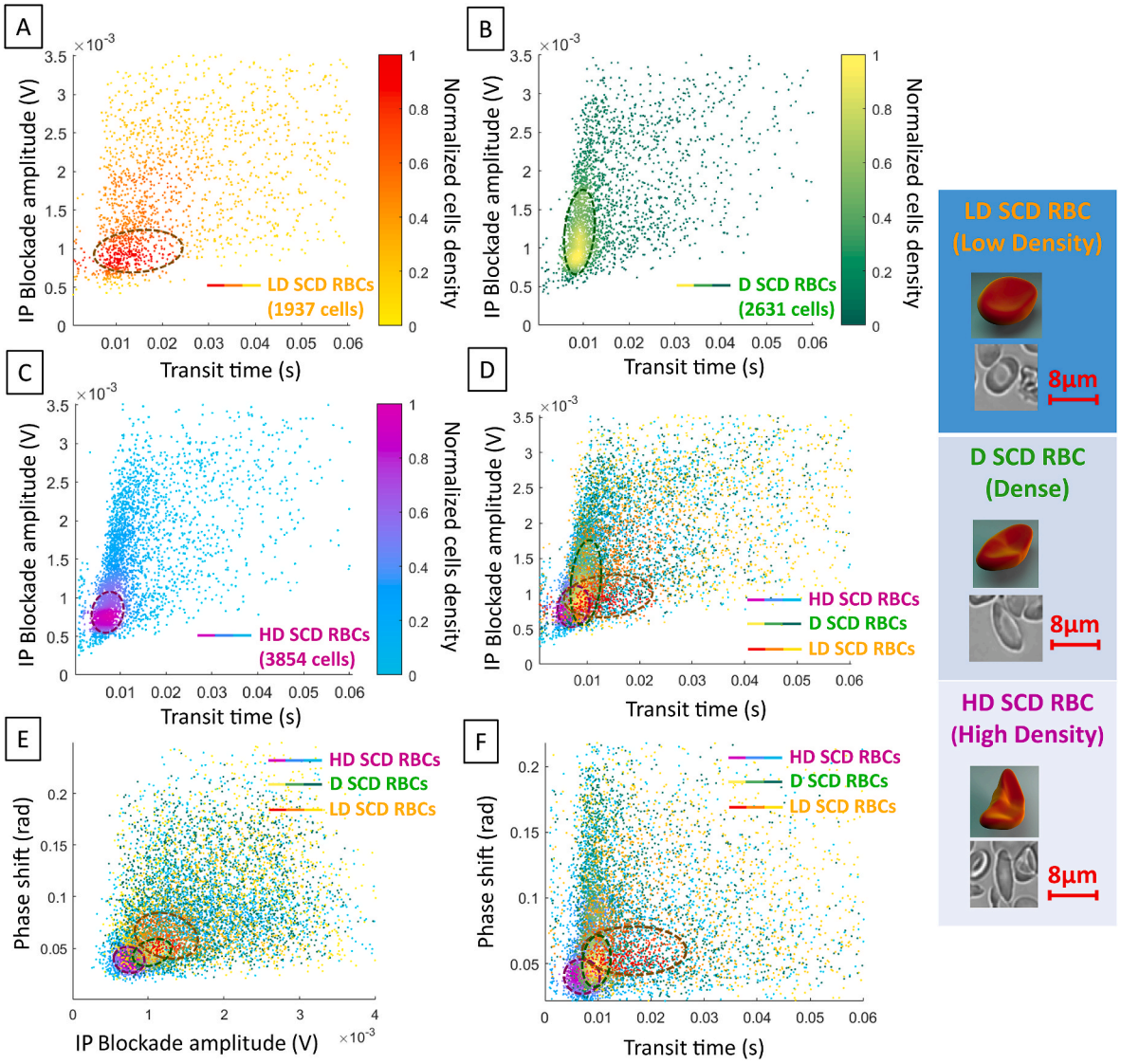

Fig. 3. Scatter plots, of IP blockade amplitude versus transit time, of phase shift versus IP blockade amplitude and of phase shift versus transit time, for each type of SCD subpopulations from three non-treated SCD patients. The color scale represents the normalized cells density. From 0 to 1, the normalized cells density increases to its maximum of each SCD cells subpopulation. The cells density was obtained by the division between the number of neighbour cells of each cell and the Voronoi area between them. Iso-density curve containing 50% of the population is also represented (dashed curve). The cell morphology observed under the microscope, as well as its 3D reconstitution are shown at the right-side of the figure for each type of sickled red blood cells (See Supplementary Table 5.). Scatter plot of IP blockade amplitude versus transit time for single SCD subpopulation: A. case of LD SCD RBCs (N = 1937); B. case of D SCD RBCs (N = 2631); C. case of HD SCD RBCs (N = 3854). Superposition of the scatter plots of three types of SCD subpopulation: D. for IP blockade amplitude versus transit time; E. for phase shift versus IP blockade amplitude; F. for phase shift versus transit time. (For interpretation of the references to color in this figure legend, the reader is referred to the Web version of this article.)

relative permittivity $\varepsilon_{memb} = 11$, negligible conductivity $\sigma_{memb} = 10^{-5}$ S/m, cytoplasm conductivity $\sigma_{cyto} = 0.9$ S/m and relative permittivity $\varepsilon_{cyto} = 50$ (Polevaya et al., 1999), the impedance measured between the pair of microelectrodes, with the presence of a single cell, can be modeled (Fig. 1D.):

$$Z_{cell} = \frac{1}{jC_{memb}\omega} + \frac{R_{cyto}}{\left(1 + jR_{cyto}C_{cyto}\omega\right)} + \frac{1}{jC_{memb}\omega}$$

where $C_{memb} = \varepsilon_0\varepsilon_{memb}\frac{S_{cell}}{e_{memb}}$, $C_{cyto} = \varepsilon_0\varepsilon_{cyto}\frac{S_{cell}}{l_{cell}}$, $R_{cyto} = \frac{1}{\sigma_{cyto}}\frac{l_{cell}}{S_{cell}}$ (S_{cell} represents the cross-sectional area of the restriction (10 μm^2), l_{cell} is the cell length contacting the surface of the microchannel), and ω represents angular frequency of the electrical excitation. The phase shift due to RBC presence in the restriction is introduced by this impedance Z_{cell}. The membrane permeability and conductivity increase with the density in our experiments, which leads to a lower phase shift also mentioned in the case of pathological cells in (Ma et al., 2012) (Sirs and Stolinski, 1970). RBC membrane thickness, relative permittivity and conductivity might depend on their pathological state, as such variation was reported in the case of heated RBC (Sirs and Stolinski, 1970). However, for our impedance detection system, we used average values from those, based on the literature.

3.4. Correlation between transit parameters

The scatter plot of IP blockade amplitude versus transit time of RBCs from the 3 SCD patients was analyzed (See Fig. 3., Supplementary Figure 7A., B., C., Supplementary Figure 8A., B. and C.). For LD RBCs, the high cell density zone (delimited by the 50% iso-density curve, see Fig. 3A.) is spreader (Fig. 3D., IP blockade amplitude versus transit time; Fig. 3E., phase shift versus IP blockade amplitude; Fig. 3F., phase shift versus transit time), probably because of the heterogeneous composition of this subpopulation in terms of reticulocytes and mature RBCs. D RBCs spread towards the higher IP blockade amplitudes (Fig. 3B.) (Lizarralde Iragorri et al., 2018). We could also confirm similarities in the deformation dynamics, by the imaging of the cell transiting through the restriction (Fig. 2, right-side, above 3D reconstitution). HD RBCs are more concentrated on the left corner of the graph (Fig. 3C., D., E. and F.), indicating a shorter detected transit time, a smaller IP blockade amplitude and a slighter phase shift.

Even though the three scatter plots of SCD subpopulations show distinct profiles, a clear overlap between these profiles is observed. This indicates that the separation of RBCs solely on the basis of cell density is not sufficient to discriminate RBCs with a specific impedance signature. This is probably because of the heterogeneity in cell size and shape among SCD RBCs of equal density, as observed by microscopy within the LD, D and HD RBC populations (Fig. 2. for RBC transit shape, Fig. 3. for RBC static shape).

Although one would expect slower circulation of RBCs in capillaries with increased density because of reduced elasticity, we found that transit time, and the two other related parameters, of SCD RBCs were inversely correlated with cell density, indicating that less deformable RBCs circulate faster in capillaries having a 5 μm × 2 μm section. This is due to the lower contact surface of D and HD RBCs with the microchannel wall of the microfluidic device. This implies that these cells would have a lower gas exchange rate with the endothelial wall *in vivo* because of reduced contact surface. The O_2 flux dependence on RBC shape diminishes as the RBC residence time increases as mentioned in (Wang and Popel, 1993) (Zarda et al., 1977). Moreover, the difference in hemoglobin (Hb) saturation at a given RBC residence time (0.22 s) can be as large as 10% for different RBC shape. However it was mentioned in those papers that at a given RBC residence time in the capillary, the RBC shape modification from normal to parachute shape induced a decrease of average O_2 flux by 26%. This suggests that, in addition to smaller oxygen cargo of sickled RBCs because of HbS polymers, altered tissue oxygenation in SCD could also be impacted by disturbed oxygen delivery because of lower contact surface area between dense RBCs and the vascular wall. The imaging of RBC morphology within the microchannel confirms the lower contact surface with higher density. Indeed, LD RBCs present a long "umbrella" shape, while D RBCs are shorter, and HD RBCs show the typical elongated sickle shape with apparent smaller contact surface with the microchannel wall.

4. Conclusion

Our miniaturized bioimpedance-microfluidic device was capable to monitor RBC microcirculatory properties, reflecting RBC size, shape and density. A clear distinction between RBC subpopulations defined by the cell density, was highlighted by our approach: mean transit time decreased with the density (from 11.5 ms to 7.4 ms) as well as IP blockade amplitude (from 1 mV to 0.8 mV) and phase shift (from 0.05 rad to 0.04 rad). Our experimental platform validates the feasibility to characterize electrically SCD RBCs under flow conditions in capillaries mimicking the *in vivo* conditions. For the future experiments, we intend to extend the study by using arrays of microelectrodes embedded in the microfluidic device to achieve a higher throughput (parallel channels) and to enable analyzing RBC parameters in successive restrictions. Such device is a promising tool to monitor the impact of therapeutical treatments on RBC behavior in the microcirculation of SCD patients.

CRediT authorship contribution statement

Tieying Xu: Methodology, Formal analysis, Investigation, Writing – original draft, Writing – review & editing. **Maria A. Lizarralde-Iragorri:** Investigation, Writing – review & editing. **Benoit Charlot:** Visualization. **Jean Roman:** Software. **Olivier Français:** Supervision, Project administration, Funding acquisition. **Wassim El Nemer:** Validation, Resources, Writing – review & editing, Supervision, Project administration, Funding acquisition. **Bruno Le Pioufle:** Resources, Writing – review & editing, Supervision, Project administration, Funding acquisition.

Declaration of competing interest

The authors declare that they have no known competing financial interests or personal relationships that could have appeared to influence the work reported in this paper.

Acknowledgements

The authors acknowledge the Labex LaSIPS (ANR-10-LABX-0040-Lasips), the "Ecole Doctorale EOBE" of Université Paris-Saclay, the "Institut d'Alembert" and the "CNRS" for project fundings. The work was supported by the Institut National de la Santé et de la Recherche Médicale (Inserm), the Institut National de la Transfusion Sanguine, the Laboratory of Excellence GR-Ex, reference ANR-11-LABX-0051, and the Laboratory of Excellence LaSIPS (ANR-10-LABX-0040-Lasips). The labex GR-Ex is funded by the IdEx program "Investissements d'avenir" of the French National Research Agency, reference ANR-18-IDEX-0001. Maria Alejandra Lizarralde Iragorri was funded by the Ministère de l'Enseignement Supérieur et de la Recherche (Ecole Doctorale BioSPC); she received financial support from: Club du Globule Rouge et du Fer and Société Française d'Hématologie.

Appendix A. Supplementary data

Supplementary data to this article can be found online at https://doi.org/10.1016/j.biosx.2022.100140.

References

Amirouche, A., Esteves, J., Lavoignat, A., Picot, S., Ferrigno, R., Faivre, M., 2020. Biomicrofluidics 14, 024116. https://doi.org/10.1063/5.0005198.

Ballas, S.K., Gupta, K., Adams-Graves, P., 2012. Blood 120, 3647–3656. https://doi.org/10.1182/blood-2012-04-383430.

Bookchin, R.M., Ortiz, O.E., Lew, V.L., 1991. J. Clin. Invest. 87, 113–124. https://doi.org/10.1172/JCI114959.

Gawad, S., Schild, L., Renaud, P., 2001. Lab Chip. https://doi.org/10.1039/b103933b.

Gee, B., Platt, O., 1995. Blood 85, 268–274. https://doi.org/10.1182/blood.V85.1.268.bloodjournal851268.

Heinrich, V., Ritchie, K., Mohandas, N., Evans, E., 2001. Biophys. J. 81, 1452–1463. https://doi.org/10.1016/S0006-3495(01)75800-6.

Hochmuth, R., Evans, C., Wiles, H., McCown, J., 1983. Science 220, 101–102. https://doi.org/10.1126/science.6828875.

Hoffman, R.A., Britt, W.B., 1979. J. Histochem. Cytochem. 27, 234–240. https://doi.org/10.1177/27.1.374580.

Kaul, D.K., Fabry, M.E., Windisch, P., Baez, S., Nagel, R.L., 1983. J. Clin. Invest. 72, 22–31. https://doi.org/10.1172/JCI110960.

Liu, J., Qiang, Y., Alvarez, O., Du, E., 2019. ACS Sens. 4, 1783–1790. https://doi.org/10.1021/acssensors.9b00263.

Lizarralde Iragorri, M.A., El Hoss, S., Brousse, V., Lefevre, S.D., Dussiot, M., Xu, T., Ferreira, A.R., Lamarre, Y., Silva Pinto, A.C., Kashima, S., Lapouméroulie, C., Covas, D.T., Le Van Kim, C., Colin, Y., Elion, J., Français, O., Le Pioufle, B., El Nemer, W., 2018. Lab Chip 18, 2975–2984. https://doi.org/10.1039/C8LC00637G.

Ma, Y.-L., Rees, D.C., Gibson, J.S., Ellory, J.C., 2012. J. Physiol. 590, 2095–2105. https://doi.org/10.1113/jphysiol.2012.229609.

Man, Y., Maji, D., An, R., Ahuja, S.P., Little, J.A., Suster, M.A., Mohseni, P., Gurkan, U.A., 2021. Lab Chip 21, 1036–1048. https://doi.org/10.1039/D0LC01133A.

Oh, K.W., Lee, K., Ahn, B., Furlani, E.P., 2012. Lab Chip 12, 515–545. https://doi.org/10.1039/C2LC20799K.

Pauling, L., Itano, H.A., Singer, S.J., Wells, I.C., 1949, 80- Science 110, 543–548. https://doi.org/10.1126/science.110.2865.543.

Piagnerelli, M., Zouaoui Boudjeltia, K., Brohee, D., Vereerstraeten, A., Piro, P., Vincent, J.-L., Vanhaeverbeek, M., 2006. J. Clin. Pathol. 60, 549–554. https://doi.org/10.1136/jcp.2006.037523.

Piel, F.B., Steinberg, M.H., Rees, D.C., 2017. N. Engl. J. Med. 376, 1561–1573. https://doi.org/10.1056/NEJMra1510865.

Polevaya, Y., Ermolina, I., Schlesinger, M., Ginzburg, B.-Z., Feldman, Y., 1999. Biochim. Biophys. Acta Biomembr. 1419, 257–271. https://doi.org/10.1016/S0005-2736(99)00072-3.

Raillon, C., Granjon, P., Graf, M., Steinbock, L., Raillon, C., Granjon, P., Graf, M., Steinbock, L., Fast, A.R., 2013. Nanoscale. https://doi.org/10.1039/c2nr30951c.

Reichel, F., Mauer, J., Nawaz, A.A., Gompper, G., Guck, J., Fedosov, D.A., 2019. Biophys. J. 117, 14–24. https://doi.org/10.1016/j.bpj.2019.05.022.

Roman, J., Le Pioufle, B., Auvray, L., Pelta, J., Bacri, L., 2018. Eur. Phys. J. E 41, 99. https://doi.org/10.1140/epje/i2018-11709-5.

Singer, S.J., Nicolson, G.L., 1972, 80- Science 175, 720–731. https://doi.org/10.1126/science.175.4023.720.

Sirs, J.A., Stolinski, C., 1970. Micron 2, 382–388. https://doi.org/10.1016/0047-7206(70)90014-2, 1969.

Steinberg, M.H., 2008. Sci. World J. 1295–1324. https://doi.org/10.1100/tsw.2008.157.

Stuart, M.J., Nagel, R.L., 2004. Lancet 364, 1343–1360. https://doi.org/10.1016/S0140-6736(04)17192-4.

Swerlick, R., Eckman, J., Kumar, A., Jeitler, M., Wick, T., 1993. Blood 82, 1891–1899. https://doi.org/10.1182/blood.V82.6.1891.bloodjournal8261891.

Toepfner, N., Herold, C., Otto, O., Rosendahl, P., Jacobi, A., Kräter, M., Stächele, J., Menschner, L., Herbig, M., Ciuffreda, L., Ranford-Cartwright, L., Grzybek, M., Coskun, Ü., Reithuber, E., Garriss, G., Mellroth, P., Henriques-Normark, B., Tregay, N., Suttorp, M., Bornhäuser, M., Chilvers, E.R., Berner, R., Guck, J., 2018. Elife 7. https://doi.org/10.7554/eLife.29213.

Varlet-Marie, E., Aloulou, I., Mercier, J., Brun, J.-F., 2010. Clin. Hemorheol. Microcirc. 44, 237–244. https://doi.org/10.3233/CH-2010-1268.

Wang, C.H., Popel, A.S., 1993. Math. Biosci. 116, 89–110. https://doi.org/10.1016/0025-5564(93)90062-f.

Ware, R.E., de Montalembert, M., Tshilolo, L., Abboud, M.R., 2017. Lancet 390, 311–323. https://doi.org/10.1016/S0140-6736(17)30193-9.

Whitesides, G.M., 2006. Nature 442, 368–373. https://doi.org/10.1038/nature05058.

Xu, T., Lizarralde-Iragorri, M.A., Roman, J., Ghasemi, R., Lefèvre, J.-P., Martincic, E., Brousse, V., Français, O., El Nemer, W., Le Pioufle, B., 2020. Sci. Rep. 10, 9869. https://doi.org/10.1038/s41598-020-66693-4.

Zarda, P.R., Chien, S., Skalak, R., 1977. J. Biomech. 10, 211–221. https://doi.org/10.1016/0021-9290(77)90044-6.

Zheng, Y., Nguyen, J., Wang, C., Sun, Y., 2013. Lab Chip 13, 3275–3283. https://doi.org/10.1039/c3lc50427a.

Zhou, Ying, Yang, D., Zhou, Yinning, Khoo, B.L., Han, J., Ai, Y., 2018. Anal. Chem. 90, 912–919. https://doi.org/10.1021/acs.analchem.7b03859.

Zhu, R., Avsievich, T., Popov, A., Meglinski, I., 2020. Cells 9, 545. https://doi.org/10.3390/cells9030545.